Internal wave breaking and mixing in the deep ocean

Marcus L. Roper

July 18, 2006

1 Introduction

We begin by outlining the two pieces of observational evidence that motivate this study.

1.1 Anomalous diffusion

The density of the abyssal ocean decreases by almost 3% from the ocean bed to the seat of the thermocline. Even when compressibility effects, such as would exist in any hydrostatically balanced fluid body, are accounted for there remains a significant potential density variation with depth, representing unequal distributions of temperature and salinity. The maintenance of this density stratification must be understood as a dynamic process. In narrow regions of the ocean at high latitudes, fluid near the ocean surface is cooled sufficiently that it becomes denser than the fluid that supports it, and sinks to great depths, mixing with entrained fluid. Accordingly, latitudinal sections of the potential density in the ocean often depict cold dense intrusions of fluid from the Antarctic or Arctic Oceans, see the Figure 1. It is estimated that in the Pacific Ocean such cold intrusions supply fluid to the lowest kilometre of ocean at a rate of 25–30 $\times 10^9\mathrm{kgs}^{-1}$ [16]. There must be a corresponding upwelling of fluid in the mid-ocean or else the centre of mass of the fluid system would be lowered with time. Such an upwelling would annihilate any variation in density, unless thwarted by downward diffusion. Specifically, if we write w for the mid-ocean upwelling velocity, we can construct an approximate balance for the two rates of density transport in the vertical direction z[1]:

$$w\frac{\partial \rho}{\partial z} \approx \kappa \frac{\partial^2 \rho}{\partial z^2} \ . \tag{1}$$

Balance in this equation leads to equilibrium distributions with a vertical scale height $H = \kappa/w$, and with $w \approx 10^{-7}\mathrm{ms}^{-1}$ and $H \approx 1\mathrm{km}$ known for the abyssal ocean, we may use this formula to estimate the effective diffusion of density: $\kappa \approx 10^{-4}\mathrm{m}^2\mathrm{s}^{-1}$ [16]. This greatly exceeds the molecular diffusivities of salt and heat (on the order of $10^{-9}\mathrm{m}^2\mathrm{s}^{-1}$ and

[1]A great deal of coarse-graining of horizontal effects, and averaging out of vertical variations must take place before this one dimensional equation may be arrived at, but the inferences drawn from it are supported by more nuanced calculations. In particular, the balance may immediately be put on a more firm footing by interpreting z as a local diapycnal coordinate – that is relating the isopycnal surface-normal components of the velocity field and diffusive flux [15].

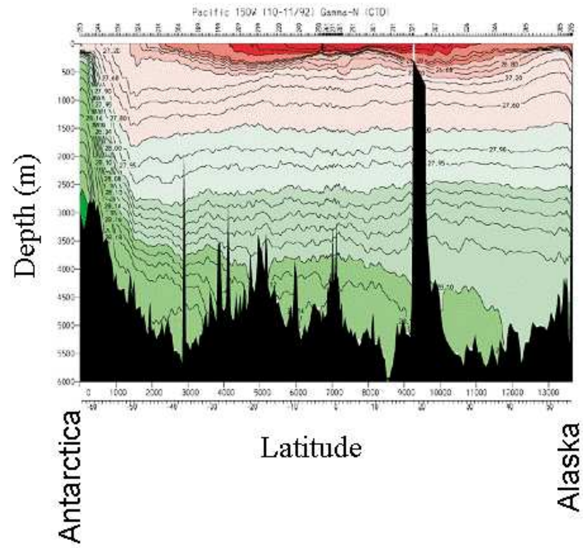

Figure 1: Potential density (σ) distribution in a section of the Pacific Ocean stretching from Antarctica (south) to the Aleutians (north). Isosurfaces are labelled by the $(\sigma - 1000) \times 10^3/\text{kgm}^{-3}$, in increments ranging from 0.20 in the thermocline to 0.02 in the ocean abyss. The black corrugations are the ocean bed. (Figure taken from [16]).

$10^{-7}\text{m}^2\text{s}^{-1}$ respectively. This disparity gives strong evidence for the dominance of other dynamical mixing processes over molecular diffusion. In the past decade strong observational evidence has emerged for enhanced eddy diffusion localised within layers of ocean hundreds of metres thick above rough or steepening regions of the ocean floor [7, 11, 13]. These mixing zones extend far beyond the turbulent boundary layer of ocean in immediate contact with the bed, signalling that the anomalous diffusion is a non-local effect: that fluid driven over the ocean floor in tidal flow, mesoscale eddies or else wave-driven currents generates internal waves which break at some distance from the ocean floor and in so doing mix up the local density field.

1.2 A universal spectrum of internal waves

The oceans are never silent, but resound with internal inertio-gravity waves at all length-scales. Compared to the energies and velocities associated with the ever-present wave field, the currents that are conventionally thought to control the global transport of temperature and salinity are in many places rather feeble. Studies by Garrett and Munk in the 1970s, culminating in [4], showed that data collected from moored, towed and dropped sensor studies of the spectrum of waves within the ocean can be united into a single common spectrum. There are various equivalent ways for casting the spectrum (see Section 2), but one common form is in terms of the horizontal and vertical wavenumbers m and k_H:

$$E(k_H, m) = \frac{3fNE_* m/m_*}{\pi(1 + m/m_*)^{5/2}(N^2k_H^2 + f^2m^2)} \tag{2}$$

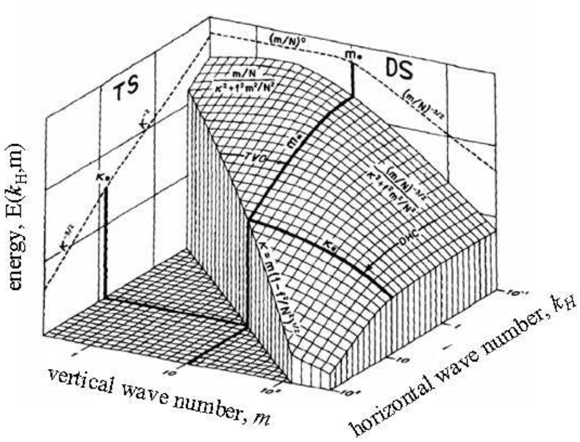

Figure 2: Energy spectrum in (k_H, m) space. Transects represent permitted observational probes of the spectrum by towed horizontal correlation (THC) and dropped vertical correlation (DVC) detecting instruments. The cleavage plane $k_H = m(1 - f^2/N^2)^{1/2}$ does not represent a physical cut-off, but is intended to clarify the plot.

where N is the buoyancy frequency, and f the frequency of purely inertial waves, and the significance of these two parameters will be discussed in Section 2. The wave-field is isotropic in any horizontal plane, so only a single horizontal wavenumber enters the relation. The spectrum is graphically shown, including various distinguished limits of small or large wavenumber, in Figure 2 drawn from [4]. The variation of the dimensional spectral density E_* and the bandwidth m_* with f (viz latitude) and N have been obtained theoretically and validated by observation [6].

The existence of a universal spectrum has become a dogma of oceanography, allowing the rate of mixing on centimetre scales to be backed out from the amount of energy in wavelengths of tens or hundreds of metres, scales which are much easier to probe experimentally. A raft of interlocking assumptions takes us from the measurements of long wavelength modes that can be relatively easily performed (using for instance acoustic Doppler profiling) to the small scale dynamics of interest. The rate of turbulent dissipation equals the rate at which energy is supplied from to the mixing scales, and this can be computed using a semi-empirical formula (see footnote 13 in [11]) comparing the mean-square shear rate, latitude and buoyancy frequency to the open ocean Garrett-Munk spectrum at a reference latitude of 30°. The rate of turbulent dissipation stands as a proxy for the dissipation of available potential energy. Total turbulent dissipation (ϵ) is assumed to exceed dissipation of available potential energy by some factor between three and five. Thus the effective diffusivity $\kappa = \Gamma\epsilon N^{-2}$, with Γ taken to be between 0.2 and 0.3. Various links in this chain of inferences have already been scrutinised theoretically (see e.g. the discussion of the use of a constant value of Γ in [10]).

1.3 Outline: A new weakly nonlinear model

In reviewing the observation evidence for a universal spectrum of internal waves, and the detailed use of this spectrum to estimate mixing rates, three questions should immediately be apparent to the reader. How can an equilibrium spectrum arise as an equilibrium state of interacting waves? How do the waves interact? How is the rate of mixing related to the energy present in the wave-field? There have been several attempts to reproduce limits of the Garrett-Munk spectrum from theoretical arguments, in particular a recent result by Lvov et al. [9] showing that the high frequency and short wavelength part of the spectrum is consistent with a model of resonant triad interactions between waves of different wavenumbers. In this report we propose a weakly nonlinear theory in which interactions between waves are viewed as spatially and temporally isolated but highly non-linear events, producing well-mixed zones of fluid. Between interactions waves evolve according to the linearised equations of motion. The use of linearised equations of motion to describe the collapse of well-mixed zones in stratified fluids is known to result in not too severe errors [1] in predictions of the density and velocity fields.

2 Evolving the linear modes

We restrict to two dimensional disturbances with uniform background stratification and no associated mean flow. We apply the Boussinesq approximation that variation in the fluid density occurs on a much longer length-scale than variation in any of the perturbation velocity fields, in which case it may be shown (see §6.4 of [5]) that the density may be taken to be constant in any evaluation of the rate of change of fluid momentum, and density variation admitted only when buoyancy forces are computed. The density field is then decomposed into three separate components: $\rho = \rho_0 + \bar{\rho}(z) + \delta\rho(x, z, t)$, and a hydrostatic component is subtracted off the pressure field to balance the background stratification $\rho_0+\bar{\rho}$.

Following §8.4 of [5], we may write down a triple of equations representing linearised momentum balance:

$$\begin{aligned} u_t - fv &= -\frac{p_x}{\rho_0} + F && \text{(3a)} \\ v_t + fu &= 0 && \text{(3b)} \\ w_t &= b - \frac{p_z}{\rho_0} + H \ , && \text{(3c)} \end{aligned}$$

where $(F,\ 0,\ H)$ are the components of a specific body force that sets the fluid into motion, $(u,\ v,\ w)$ is the disturbance velocity field, and $b = -\frac{g\delta\rho}{\rho_0}$ the buoyancy field. The dynamical effect of the rotating frame has been trammelled up into the pair of Coriolis force terms on the right-hand side of (3), in which we have followed convention by defining a parameter $f = 2\Omega$: centrifugal terms are assumed to have been assimilated into a redefined gravitational acceleration g.

Mass continuity then takes linearised form:

$$b_t + N^2 w = 0 \ , \tag{4}$$

while, consistent with the Boussinesq approximation, we may assume that fluid parcels neither gain nor lose mass as they are advected by the fluid, giving rise to the standard incompressibility relation:

$$u_x + w_z = 0 \ . \tag{5}$$

We make immediate use of the incompressibility equation by defining a streamfunction ψ such that $u = \psi_z$, $w = -\psi_x$, allowing us to reduce the number of time-evolution equations by one. Specifically, subtracting the x-derivative of (3c) from the z-derivative of (3a) gives the vorticity equation:

$$\nabla^2 \psi_t - f v_z = -b_x + \tau \ , \tag{6}$$

where $\tau \equiv F_z - G_x$ is the specific torque associated with the body force posited above. We define a *potential temperature* for the fluid:

$$\theta \equiv -\frac{g(\rho - \rho_0)}{\rho_0} = N^2 z + b \tag{7}$$

so that the disturbed fluid is stably or unstably stratified according to whether $\theta_z \gtrless 0$.

We scale lengths by the horizontal and vertical dimensions of our experimental box (L_x, L_z), defining dimensionless hatted variables $z = L_z \hat{z}$, $x = L_x \hat{x}$. We also define an aspect ratio $\epsilon \equiv L_z / L_x$, which we anticipate being small. It is natural to scale the buoyancy field using the background potential temperature: $b = N^2 L_z \hat{b}$, and the time by the buoyancy period $t = \hat{t}/N$, which will turn out to be the minimum period of any of the linear inertia-gravity wave modes of the fluid body. Scalings for the other dynamical variables follow from selecting dominant balances between pairs of terms in the vorticity and mass conservation equations. Balancing the rate of increase of vorticity ψ_{zzt} with the rate of baroclinic generation b_x, suggests a scaling for the velocity fields: $\psi = \epsilon N L_z^2 \hat{\psi}$, and we scale v to balance the y-component of the fluid acceleration v_t with the Coriolis force fu: $v = \epsilon^2 N L_z$. To ensure that the specific torque term participates in the dominant balance of terms in the vorticity equation set $\tau = \epsilon N^2 \hat{\tau}$. We drop the hat decorations straightaway, and present in dimensionless form our remaining governing equations:

$$\begin{aligned} \left(\epsilon^2 \frac{\partial^2}{\partial x^2} + \frac{\partial^2}{\partial z^2}\right) \psi_t - \epsilon \, \mathrm{Pr} \, v_z + b_x &= \tau && \text{(8a)} \\ \epsilon v_t + \mathrm{Pr} \, \psi_z &= 0 && \text{(8b)} \\ b_t - \epsilon^2 \psi_x &= 0 \ . && \text{(8c)} \end{aligned}$$

Here $\mathrm{Pr} \equiv f/N$ is sometimes called the *Prandtl ratio*, and encodes the relative strengths of buoyancy to inertial forces. It is natural to take $\epsilon = \mathrm{Pr}$, i.e. to consider a box with aspect ratio dictated by the balance between rotational stiffness in the horizontal direction (the tendency of fluid to move in Taylor columns), and stratification stiffness in the vertical (resisting any lifting of isopycnal surfaces). A typical deep ocean value of the Prandtl ratio is $\mathrm{Pr} = 0.1$.

2.1 Unforced modes

With F and H set to zero, the fluid body supports free inertiogravity waves. It suffices to consider the evolution of plane-wave disturbances, with well defined wavenumber $\boldsymbol{k} =$

$(k,\ 0,\ m)$. The time evolution of the $(\psi,\ v,\ b)$ fields must satisfy the triplet of equations:

$$-(\epsilon^2 k^2 + m^2)\psi_t - i\epsilon \,\mathrm{Pr}\, mv + ikb = 0 \quad (9a)$$

$$\epsilon v_t + im\,\mathrm{Pr}\,\psi = 0 \quad (9b)$$

$$b_t = i\epsilon^2 k\psi\ . \quad (9c)$$

Since there is no explicit time dependence in these equations, we are allowed to seek solutions with monochromatic time dependence: $(\psi,\ v,\ b) \propto e^{-i\omega(\boldsymbol{k})t}$ for some eigenfrequency ω. Determination of the eigenvalues and eigenvectors of the associated linear operator reveals the existence of three unforced modes of the body:

(i) A *geostrophically balanced* steady mode, with $\omega = 0$. The pressure field is hydrostatic $p_z/\rho_0 = b$, and the y-component of the velocity field fixed by the Coriolis-buoyancy balance in (3a):

$$\psi_b = 0 \quad \text{and} \quad kb_b = \epsilon\,\mathrm{Pr}\, mv_b\ . \quad (10)$$

(ii),(iii) Two propagating modes with frequencies

$$\omega_\pm(\boldsymbol{k}) = \pm\sqrt{\frac{\mathrm{Pr}^2 m^2 + \epsilon^2 k^2}{m^2 + \epsilon^2 k^2}}\ , \quad (11)$$

with wave-components

$$\mathrm{Pr}\, m\psi_\pm = \pm\epsilon\omega_\pm v_\pm \quad \text{and} \quad \mathrm{Pr}\, mb_\pm = -\epsilon^3 kv_\pm\ . \quad (12)$$

With a little algebra, we see that an arbitrary initial disturbance may be decomposed into balanced and propagating wave fields as:

$$\psi_b = 0 \quad b_b = \frac{\mathrm{Pr}^2 m^2 b + \epsilon^3 k\,\mathrm{Pr}\, mv}{\mathrm{Pr}^2 m^2 + k^2\epsilon^2} \quad v_b = \frac{k\,\mathrm{Pr}\, mb + \epsilon^3 k^2 v}{\epsilon\left(\mathrm{Pr}^2 m^2 + \epsilon^2 k^2\right)}\ , \quad (13)$$

with

$$\psi_\pm = \frac{1}{2}\left(\psi \mp \frac{\omega kb - \epsilon\omega\,\mathrm{Pr}\, mv}{\mathrm{Pr}^2 m^2 + \epsilon^2 k^2}\right) \quad b_\pm = \frac{1}{2}k\epsilon^2\left(\mp\frac{\psi}{\omega} + \frac{kb - \epsilon\,\mathrm{Pr}\, mv}{\mathrm{Pr}^2 m^2 + \epsilon^2 k^2}\right)\ , \quad (14)$$

and

$$v_\pm = \frac{1}{2\epsilon}\left(\pm\frac{\mathrm{Pr}\, m\psi}{\omega} - \frac{k\,\mathrm{Pr}\, mb - \epsilon\,\mathrm{Pr}^2 m^2 v}{\mathrm{Pr}^2 m^2 + \epsilon^2 k^2}\right)\ ; \quad (15)$$

where we have identified $\omega \equiv \omega_+$, and note that such modes can then be evolved with time analytically. Note that the above expressions are singular if both k and m vanish: this corresponds to static raising or lowering of the entire body of fluid.

2.2 Forced modes

Grave modes of the system are forced by some external agency. To avoid imparting unwanted spatial or temporal structure to the disturbance thereby set up, we assume white noise forcing. Each mode may therefore include a forced component:

$$\frac{\partial}{\partial t}\begin{pmatrix}\psi\\ b\\ v\end{pmatrix} = \begin{pmatrix} -\frac{i\epsilon\,\mathrm{Pr}\, m}{m^2+\epsilon^2k^2} & 0 & \frac{ik}{m^2+\epsilon^2k^2}\\ 0 & i\epsilon^2 k & 0\\ 0 & -\frac{i\,\mathrm{Pr}\, m}{\epsilon} & 0\end{pmatrix}\begin{pmatrix}\psi\\ b\\ v\end{pmatrix} - \frac{\tau}{m^2+\epsilon^2k^2}\begin{pmatrix}1\\ 0\\ 0\end{pmatrix}\ . \quad (16)$$

where, by appropriate choice of the unforced component, it suffices to consider the initial conditions $\psi = b = v = 0$ at $t = 0$. Now, it can easily be seen that the form of the forcing is such as to never excite the geostrophically balanced mode, so that any forced mode can be instantaneously decomposed into contributions from the two propagating eigenmodes. Supposing that we have not chosen to force a mode with vanishing vertical wavenumber (although the extension to such purely buoyancy driven waves is trivial) it is convenient to chart the evolution of these two modes via the v-amplitudes:

$$v_\pm(t) = \mp \frac{\mathrm{Pr}\, m}{2\epsilon\omega(\epsilon^2 k^2 + m^2)} \int_0^t e^{\pm i\omega(s-t)} \tau(s)\, \mathrm{d}s \ , \tag{17}$$

where for white noise forcing the integration measure may be written as $\tau(s)\,\mathrm{d}s = \tau_0(\mathrm{d}W_{1s} + i\mathrm{d}W_{2s})$, where τ_0 is some constant representing the strength of the forcing, and W_{1s}, W_{2s} are independent Wiener-processes. We therefore see that $v_\pm(t)$ are both (complex-valued) Gaussian random variables, with easily computable mean and expectations. A little algebra then gives the evolution of the forced modes:

$$v(\boldsymbol{k},t) = X(\boldsymbol{k},t) \ , \quad b(\boldsymbol{k},t) = -\frac{\epsilon^3 k}{\mathrm{Pr}\, m} X(\boldsymbol{k},t) \quad \text{and} \quad \psi(\boldsymbol{k},t) = \frac{\epsilon\omega}{\mathrm{Pr}\, m} Y(\boldsymbol{k},t) \ , \tag{18}$$

where X and Y are complex Gaussian random variables with covariance matrix:

$$\mathbb{E}\begin{pmatrix} \Re X \\ \Im X \\ \Re Y \\ \Im Y \end{pmatrix}\begin{pmatrix} \Re X \\ \Im X \\ \Re Y \\ \Im Y \end{pmatrix}^T = \frac{\mathrm{Pr}^2\, m^2 \tau_0^2}{\epsilon^2\omega^2(m^2+\epsilon^2k^2)^2} \times$$
$$\begin{pmatrix} \frac{1}{2}\left(t - \frac{1}{2\omega}\sin 2\omega t\right) & 0 & 0 & \frac{1}{4\omega}(1-\cos 2\omega t) \\ 0 & \frac{1}{2}\left(t - \frac{1}{2\omega}\sin 2\omega t\right) & \frac{1}{4\omega}(1-\cos 2\omega t) & 0 \\ 0 & \frac{1}{4\omega}(1-\cos 2\omega t) & \frac{1}{2}\left(t + \frac{1}{2\omega}\sin 2\omega t\right) & 0 \\ \frac{1}{4\omega}(1-\cos 2\omega t) & 0 & 0 & \frac{1}{2}\left(t + \frac{1}{2\omega}\sin 2\omega t\right) \end{pmatrix} \tag{19}$$

The stochastic evolution of the forced linear modes can therefore also be performed analytically. It will be necessary in diagnosing the proximity of the system to an equilibrium state to relate the rate at which energy is supplied to the system by white-noise forcing, to the rate of dissipation in breaking events. As an intermediate step to doing this, it is useful to write down an energy balance the distribution of energy between system modes:

$$\frac{1}{2}\frac{d}{dt}\sum_{\boldsymbol{k}} \left(|b(\boldsymbol{k})|^2 + \epsilon^4|v(k)|^2 + \epsilon^2(\epsilon^2k^2+m^2)|\psi(\boldsymbol{k})|^2\right) = \epsilon^2 \sum_{\boldsymbol{k}} \tau(\boldsymbol{k})\psi(-\boldsymbol{k}) \tag{20}$$

the first term on the left hand side gives the available potential energy of the system (the amount of energy that would be liberated if the preexisting stratification were restored), and the remaining two terms the kinetic energy for out-of-plane and in-plane motion respectively. For freely propagating disturbances it may be shown that energy is equipartitioned between the first pair of terms and the third.

3 Wave-breaking

Large amplitude wave-disturbances are vulnerable to both shear and Rayleigh-Taylor instabilities. In general these two mechanisms act together. Many experimental, numerical and theoretical studies have addressed the cascade of instabilities in a linearly stratified shear layer. It is known that for simple shear flows, shear instabilities set in only if the Richardson number ($\mathrm{Ri} = N^2/u_z^2$) does not exceed 1/4 [8], and direct numerical simulations have tracked the instabilities then produced, starting with the formation of Kelvin-Helmholtz billows that overturn the stratification gradient, and followed by production of streamwise eddies [12]. However, this Richardson number criterion is known not to be an accurate predictor of instability in other flow configurations [3], and the Reynolds numbers for which accurate simulations of the instability-induced mixing are feasible remain an order of magnitude below those seen in the ocean. Regardless of the obscurity of the conditions needed for instability and of the kinematics of mixing, experiments [8] and observations of atmospheric clear-air turbulence [3, figure 5] give a clear and consistent picture of the effect of mixing upon the stratification in a fluid: compact patches of well-mixed fluid are produced (with stratification obliterated) and gravity waves shed into the surrounding medium. The mixed patches are typically surrounded by layers of steeply stratified fluid, giving rise to an easily identified "rabbit-ear" signature in radiosonde studies of the thermal profile, which would correspond to sharp spikes in N^2 in our system.

We introduce a simple diffusive model for the mixing of fluid by a breaking gravity wave. Mixing is taken to occur whenever the fluid becomes gravitationally unstable (so that at some site $\theta_z < 0$), with no accounting for shear enhancement. The mixing time-scale is assumed to be much smaller than the period of the wave that triggered mixing, so that the continuing evolution of the wave-field can be halted while mixing occurs. For simplicity, mixing is assumed only to redistribute fluid mass so that the Eulerian distribution of velocity is *frozen in* during mixing. This is unphysical, but allows the question of parametrising the turbulent dissipation of kinetic energy to be side-stepped. To select a diffusive model we impose the following constraints:

(i) Mixing must be energy-dissipative. Since the velocity field is unaffected by mixing, this means that the available potential energy must decrease monotonically with time.

(ii) Mixing zones must have compact support, and must include all regions of fluid in which $\theta_z < 0$.

(iii) Density must be exactly conserved at all times.

(iv) Mixing must terminate upon reaching a stably stratified state. The mixing scheme should produce well-mixed zones, rather than set up a stable stratification.

(v) The "rabbit ear" structure should be reproduced in the layers of fluid surrounding mixed-zones.

Constraints (ii)-(iv) point towards a diffusive scheme in which the diffusive flux is proportional to the gradient in the potential temperature rather than buoyancy (that is $\boldsymbol{J} \propto -\nabla\theta$, rather than $\propto -\nabla b$). A simple candidate scheme has:

$$\frac{\partial b}{\partial T} = \nabla \cdot (D[\theta_z]\nabla\theta) \quad \text{with} \quad D[\theta_z] = -H(-\theta_z)\theta_z \ . \tag{21}$$

Here the $H(x)$ is the Heaviside function, and we have introduced a mixing-time variable T. In our scaled geometry $\nabla = \left(\epsilon\frac{\partial}{\partial x}, \frac{\partial}{\partial z}\right)$. Check that property (i) is satisfied: Multiplying

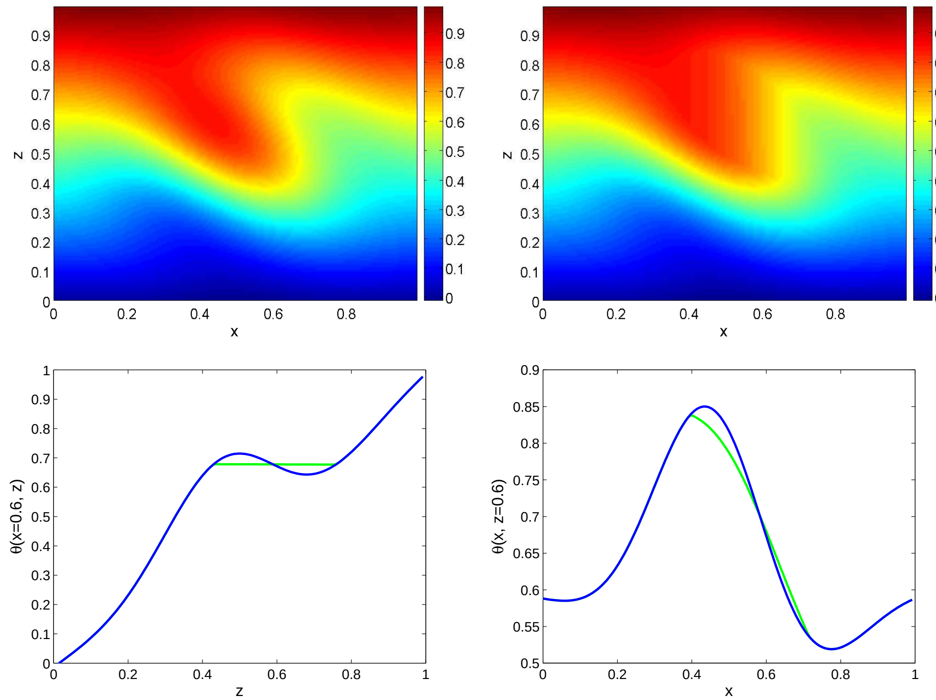

Figure 3: Diffusive scheme applied to the unstable buoyancy profile: $b(x,z) = 0.3\exp[-((x-0.5)^2 + (z-0.5)^2)/0.09]\cos[2\pi(x+z)]$. (a) (b) are surface plots of the potential temperature distribution before and after mixing. (c) and (d) give potential temperature profiles on the transects $x = 0.6$ and $z = 0.6$ respectively. The blue curve is the profile before mixing, and the green curve is the profile after mixing.

both sides of (21) by b and integrating over the entire of the fluid domain, we have

$$\frac{d}{dt}\,\frac{1}{2}\int b^2 \mathrm{d}x\mathrm{d}z = -\int D[\theta_z]\left(\frac{\partial b}{\partial z} + |\nabla b|^2\right)\mathrm{d}x\mathrm{d}z < 0 \tag{22}$$

since by construction $D \equiv 0$ except where $\partial b/\partial z < -1$. In integrating by parts and discarding boundary contributions, we have made tacit use of the fact that periodic boundary conditions will be imposed upon b. Physically we expect strong diffusion initially in zones where $\theta_z < 0$, but that diffusivity will bleed away with time, leaving patches of uniform θ (in z if not in x). An example of the application of this diffusive mixing scheme to an initially unstable density profile is shown in Figure 3. Note that for typical aspect ratios ($\epsilon \approx 0.1$) density is almost conserved at each x-station. At x-stations with a single density inversion (i.e. interval in which $\theta_z < 0$) this means that the mixing produces a Maxwell-type construction, with the density made uniform in the smallest z-interval that contains the unstable zone, while conserving total fluid mass and giving a continuous final density distribution (see Figure 3c). The weakness of density diffusion between x-stations means that density distribution is markedly less smooth on horizontal sections than on vertical sections (see Figure 3d). This is intuitively appealing: although the breaking inertiogravity waves respect the x and z scalings introduced here, Coriolis forces act only weakly upon the turbulent eddies generated during wave breaking, so that we expect mixing to be isotropic in the *unscaled* x and z coordinates.

Note that condition (v) is not satisfied by the diffusive scheme (21) which always produces continuous θ profiles, and does not in general enhance the stable θ gradients surrounding a mixing zone. One remedy for this would be to extend the support of the diffusivity function D to include some region of stably stratified fluid. Ensuring that this is compatible with the dissipative condition (i) is difficult. In the direct numerical simulation literature the *Thorpe displacement* is sometimes invoked for this purpose [12]. The Thorpe displacement $d(z;x)$ is defined for the column of fluid occupying each of the x-stations, as the minimum distance that the fluid particle at z must be moved in a vertical reordering of the fluid particles in the column to create a stable stratification. It has been suggested that at any instant the region in which turbulent overturning must occur can be identified with the part of the fluid having non-zero Thorpe displacement [2]. However, one may easily construct examples in which diffusion over the entire zone of non-zero Thorpe displacement would lead to a gain in available potential energy, in violation of condition (i). A more promising approach attempts a more careful budgeting of the energy available for mixing from both the kinetic energy and available potential energy of the flow. The diffusivity D is identified with the amount of turbulent energy present, and is allowed to self-diffuse. Zones of fluid in which $\theta_z \lesseqgtr 0$ are treated as diffusivity sources and sinks respectively. While these models allow diffusion over significantly larger fluid regions than (21) and may therefore satisfy (v), and can be constructed so as to conserve [14] or dissipate energy, they also require the addition of multiple ill-constrained parameters for the separate diffusivities of density, momentum and turbulent energy.

4 Numerical implementation

A cartoon of the numerical scheme for combining linear evolution (§2) with diffusive mixing (§3) is given in Figure 4.

We describe briefly some of the numerical desiderata. We impose periodic boundary conditions upon the b, ψ and v fields, and discretise the numerical domain with a grid of M points in the x direction and N points in the z-direction. Typically we let M and N range from 32 up to 256. Fast Fourier Transforms are used to pass between physical and wavenumber representations of the wave fields. The time interval Δt over which the fields are allowed to evolve between mixing events is held fixed throughout the simulation, so that the evolution of the unforced components can be determined in advance by the computation of time evolution operators $\exp(\mp i\omega(\boldsymbol{k})\Delta t)$ for each of the modes. Stochastic evolution of the forced modes requires us to generate the Gaussian random variables X and Y that feature in the equation (18). We do this by calculating the covariance matrix (denoted by $C(\Delta t;\boldsymbol{k})$) for $(\Re X, \Im X, \Re Y, \Im Y)$, and finding its Cholesky decomposition $C \equiv LL^T$. The requisite X, Y at each time step may then be generated as $(\Re X, \Im X, \Re Y, \Im Y) = L\boldsymbol{\xi}$, where $\boldsymbol{\xi}$ is a quadruple of $N(0,1)$ random variables.

For the implementation of the diffusive mixing step, spatial derivatives are approximated by second order centred differences, and the time stepping is performed with a fully implicit second order scheme (the Matlab routine `ode23s`, based on the Rosenbrock formula, which

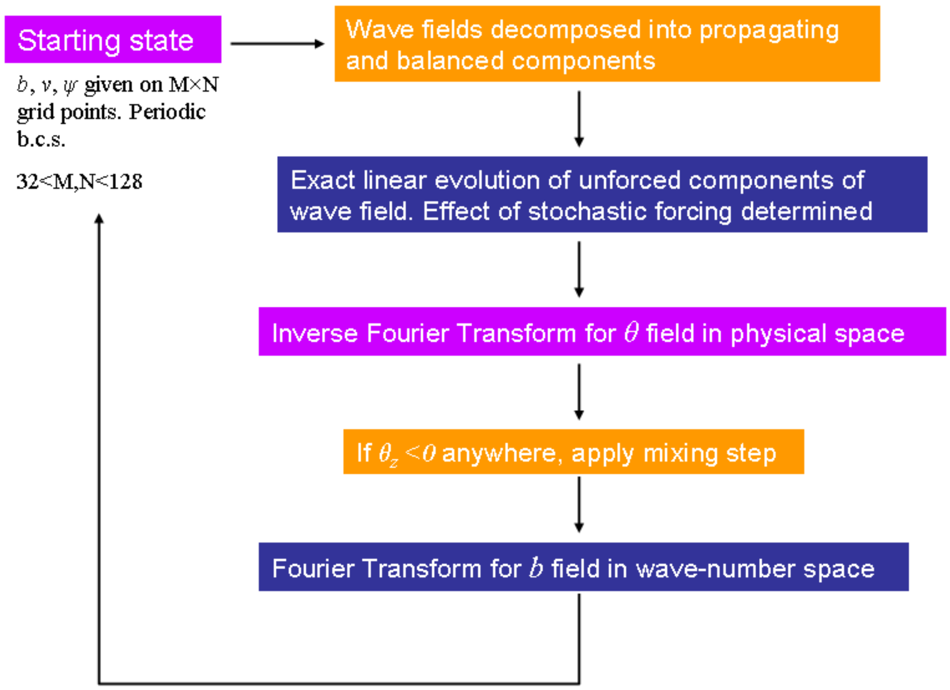

Figure 4: A numerical scheme for combining linear evolution with diffusive mixing.

we have altered to make use of UMFPACK to perform an LU-factorisation of the large but sparse Jacobian matrix). To ensure that the associated system of time equations have a well-defined Jacobian it is necessary to smooth the Heaviside function term appearing in the diffusivity. In practice we use:

$$H(x) \approx \frac{1}{2}\left(x + \sqrt{x^2 + 4\epsilon}\right) \ , \tag{23}$$

where the smoothing length ϵ is set at machine precision $\epsilon \approx 10^{-12}$ without any evident irregularity in the running of the code. Diffusion was terminated when θ_z exceeded some critical value (typically -0.005) throughout the fluid domain. Numerical results for the mixing step were tested using a finite element package (COMSOL Multiphysics 3.2).

There are two fundamentally different experiments that can be performed using the numerical scheme described here. In the first, *relaxation*, all wavenumbers are initially given identical energies, randomly allocated between leftward and rightward propagating modes, and with uniformly randomly distributed phases for each component. The system is then allowed to evolve without forcing until it reaches equilibrium with, in the end stages, exponential decay in the total energy, and increase in the waiting time between mixing events. In the second experiment, *build-up*, one or two of the gravest modes of the system are supplied with white noise forcing, and the transmission of energy from these modes to other modes is charted.

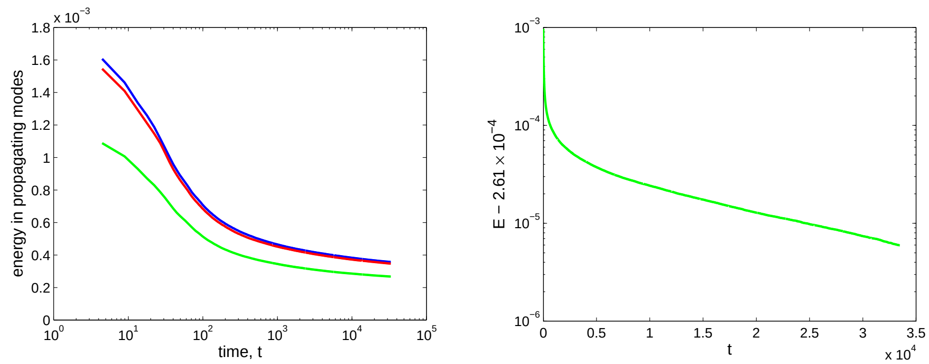

Figure 5: (a) Effect of varying initial state. The three curves give relaxation dynamics of system starting with different random initial states. (b) Green data set replotted on log-log scale. All simulations are run with $M = N = 64$.

5 Results

5.1 Relaxation experiments

The *effect of the initial state* upon the evolution of the system is shown in Figure 5a. Only the energy in propagating modes is plotted - the contribution from geostrophically balanced modes is an order of magnitude smaller. In part b of the figure, one of the data sets is replotted on a linear-log scale to show the exponential convergence of the total wave energy. It can be seen that the initial state is not forgotten, but helps to determine the total energy that the system relaxes to. Two systems with initially closely separated energies ultimately equilibrate with similar energies, as the red and blue curves show.

Phase structure in evolved states. It must be asked whether the equilibrium states of the system have definite phase as well as energy spectra - i.e. that the different wave components must have specific phase lags to avoid constructive interference that may lead to breaking. We test for this by taking one of the late time system states from Figure 5a, randomising all of the phases and allowing it to evolve with time, to see if the equilibrium is altered. Results are shown in Figure 6. It is seen that the apparent equilibrium energy of the propagating modes (which is found by fitting the energy-time curve to a decaying exponential and extrapolating to infinity) varies by less than 2%. This suggests that the equilibrium phase spectrum of the system is white.

The *effect of varying the time-interval between mixing events* is shown in Figure 7, in which an identical initial state is let evolve three times, with different time intervals Δt between mixing events for each of the iterations. The energy of the system is sensitive at early times to the value of Δt, but not the value of energy that the system ultimately converges to. Smaller values of Δt give faster convergence to the equilibrium energy.

Evolved spectra. In Figure 8 we compute the detailed distribution of energy among wave-modes for the green data set from Figure 5. The spectra corresponding to other data sets are qualitatively similar, and we are developing methods for direct comparison. The redness of the spectrum is similar to that of the Garrett-Munk spectrum, although lack of resolution

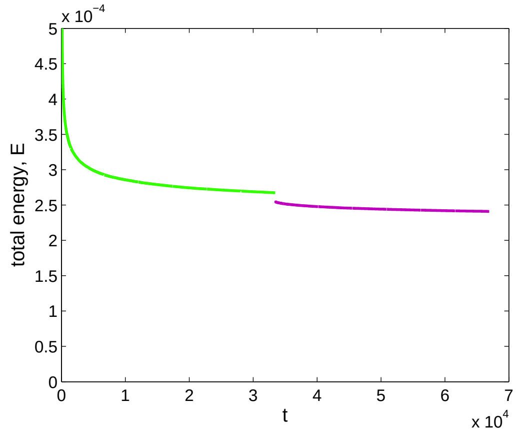

Figure 6: Effect of randomisation of phase of wave modes upon the relaxation of a system to equilibrium. Green curve shows initial evolution (identical to the green data set in Figure 5), and purple curve the continuing evolution after phases are randomised at a time $t = 3.3 \times 10^4$.

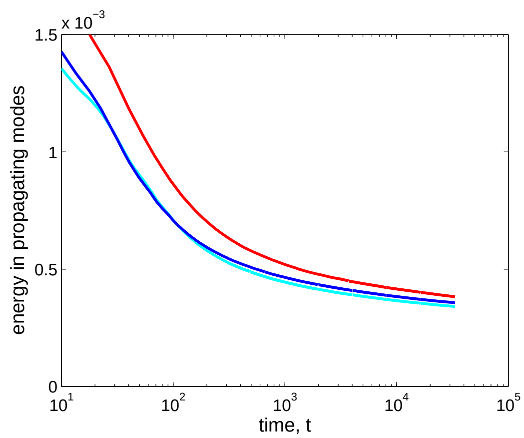

Figure 7: Effect of varying time interval between mixing events upon relaxation dynamics. Red curve corresponds to $\Delta t = 13.40$, blue curve to $\Delta t = 4.46$, and cyan curve to $\Delta t = 1.12$ (all times are measured in units of $1/N$).

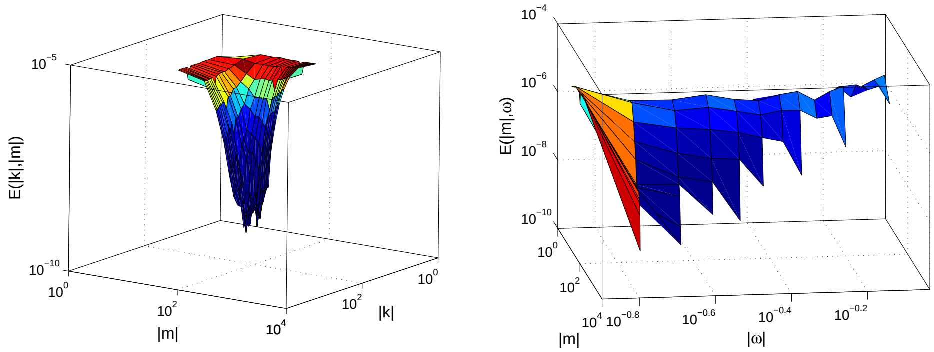

Figure 8: Relaxation spectra in (a) $(|k|,|m|)$ and (b) $(|m|,|\omega|)$ space.

prevents direct comparison of the scalings for the inertial peaks. The spectrum is also peaked at small m (corresponding to purely buoyancy driven waves) in visible disagreement with the GM spectrum. These modes correspond to lifting of vertical columns of fluid, and do not therefore participate in breaking: either in determining whether breaking will occur, or in mixing, because, as was discussed in §3, this mainly leads to vertical transport of mass. The persistence of these modes, once excited, is a knotty problem for the model.

5.2 Build-up experiments

It is not feasible to force a single mode of the system, since any spatial periodicity of the forced mode will be inherited by the modes created during wave breaking, leading to a sparse energy spectrum. To break this symmetry we force a *pair* of grave modes $(k,m) = (2\pi, \pm 2\pi)$ with the same forcing constant τ_0, and the first mode initially just below its breaking amplitude and the second mode started from zero amplitude. It is also necessary to impose an adiabaticity constraint upon the forcing, that the time taken for the forcing to bring the forced mode to breaking must greatly exceed the period of the mode, i.e. that:

$$\tau_0 \ll \left(\frac{\omega^3}{2\pi}\right)^{1/2} \frac{m^2 + \epsilon^2 k^2}{\epsilon^2 km} \; . \tag{24}$$

For τ_0 significantly greater than this threshold value, the energy in the forced modes is observed to grow without bound. Wave-breaking only removes energy from the buoyancy field, and we can only be assured that energy is equipartitioned between the available potential energy (plus the out-of-plane kinetic energy) and the in-plane kinetic energy if the adiabaticity condition is met.

It can be seen that the energy spectrum is dominated by the handprint of the forced modes. These modes remain saturated (at the brink of breaking) and transmission of energy to other modes is inefficient. In Figure 9a we show the total energy budget for one realisation of this system, showing that that it attains a flux-dissipative equilibrium (with the rate of dissipation by mixing equal to the energy input from the white noise). Experimentally the mean energy value in this equilibrium depends upon the particular modes being forced, but not upon the strength of the forcing τ_0 or upon the time between mixing events Δt.

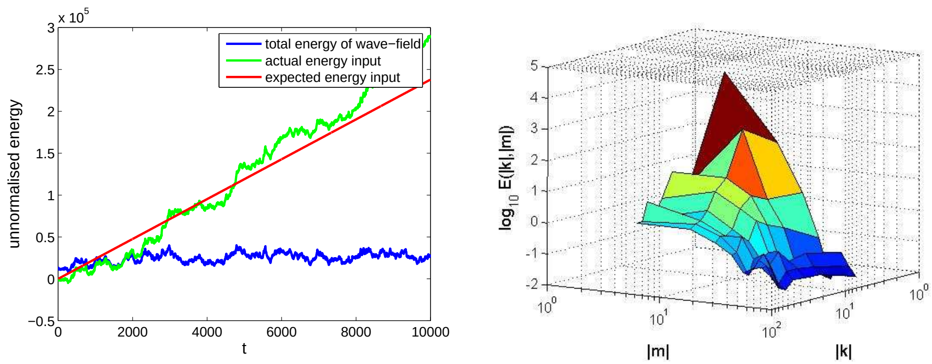

Figure 9: (a) Energy budget for forced mode, showing rate of energy input from white noise, against total energy of all wave modes. (b) Time-averaged energy spectrum when system has attained flux-dissipative equilibrium. Simulations were run on an older version of the code, on an $M = N = 2^5$ grid, with unnormalised energies (which must be divided by $M^2N^2 = 2^20$ for comparison with Figure 5) and anisotropic diffusion (setting $\nabla = (\partial/\partial x,\, \partial/\partial z)$ in (21)), but are in qualitative accord with experiments using the modified code described in this report.

The rate of energy increase in unforced modes is slow, and it is unclear whether a forced-dissipative equilibrium has actually been reached by the end of the simulation. In truth Figure 9a probably represents no more than the achievement of a flux-dissipative equilibrium for the single forced mode of the system. In Figure 9b we show the (coarsely-binned) energy spectrum of the system as a function of wave-number, showing clear peaking at the forced wavelengths. It may be possible to clarify whether equilibrium has been attained by running a hybrid of the relaxation and build-up experiments, in which the other modes are given some initial energy and allowed to *relax to* rather than *build up to* a steady state.

6 Discussion

Basic questions about the capabilities and limitations of the model remain unasked. The preliminary simulations described here show that a large number of energy equilibria can be accessed when an unforced wave-field is allowed to relax from some higher-energy initial state. These states appear to all have structure-free phase spectra and relatively homologous energy spectra, suggesting that the family of equilibrium states could be parametrised by their total energy, and we are in the process of running simulations to simulate relaxation for a large assay of initial states at a higher resolution, in order to confirm this. The problem of the persistence of $m = 0$ states remains unresolved. Results of the *build-up* simulations are less promising - a method must be found to subtract out the forced mode from the final spectra (Figure 9), or for hastening the equilibration of these modes. Incorporation of forcing is vital to our efforts to use the model to tackle the problem of anomalous diffusion (§1.1), since the rate of mixing will be ultimately controlled by the rate of energy input into the wave-field.

The author thanks Oliver Bühler for guidance over the duration of the GFD summer school, and gratefully acknowledges discussions with Neil Balmforth, Paul Milewski, Esteban Tabak and Bill Young.

References

[1] O. Bühler, M. E. McIntyre, and J. F. Scinocca, *On shear-generated gravity waves that reach the mesosphere. Part I: Wave generation*, J. Atmos. Sci., 56 (1999), pp. 3749–3763.

[2] P. J. Diamessis and K. K. Nomura, *The structure and dynamics of overturns in stably stratified homogeneous turbulence*, J. Fluid Mech., 499 (2004), pp. 197–229.

[3] D. C. Fritts, C. Bizon, J. A. Werne, and C. K. Meyer, *Layering accompanying turbulence generation due to shear instability and gravity-wave breaking*, J. Geophys. Res. D, 108 (2003), pp. PMR 20–1.

[4] C. Garrett and W. Munk, *Internal waves in the ocean*, Ann. Rev. Fluid Mech., 11 (1979), pp. 339–369.

[5] A. E. Gill, *Atmosphere-Ocean Dynamics*, Academic Press, San Diego, 1982.

[6] M. C. Gregg, T. B. Sanford, and D. P. Winkel, *Reduced mixing from the breaking of internal waves in equatorial waters*, Nature, 422 (2003), pp. 513–515.

[7] J. R. Ledwell, E. T. Montgomery, K. L. Polzin, L. C. S. Laurent, R. W. Schmitt, and J. M. Toole, *Evidence for enhanced mixing over rough topography in the abyssal ocean*, Nature, 403 (2000), pp. 179–182.

[8] P. F. Linden, *Mixing in stratified fluids*, Geophys. Astro. Fluid Dyn., 13 (1979), pp. 3–23.

[9] Y. V. Lvov, K. L. Polzin, and E. G. Tabak, *Energy spectra of the ocean's internal wave field: Theory and observations*, Phys. Rev. Lett., 92 (2004).

[10] M. E. McIntyre, *On dynamics and transport near the Polar Mesopause in summer*, J. Geophys. Res. D, 94 (1989), pp. 14617–14628.

[11] A. C. Naveira Garabato, K. L. Polzin, B. A. King, K. J. Heywood, and M. Visbeck, *Widespread intense turbulent mixing in the southern ocean*, Science, 303 (2004), pp. 210–213.

[12] W. R. Peltier and C. P. Caulfied, *Mixing efficiency in stratified shear flows*, Ann. Rev. Fluid Mech., 35 (2003), pp. 135–167.

[13] K. L. Polzin, J. M. Toole, J. R. Ledwell, and R. W. Schmitt, *Spatial variability of turbulent mixing in the abyssal ocean*, Science, 276 (1997), pp. 93–96.

[14] E. G. Tabak and F. A. Tal, *Mixing in simple models for turbulent diffusion*, Comm. Pure Appl. Math., 57 (2004), pp. 563–589.

[15] K. B. Winters and E. A. D'Asaro, *Diascalar flux and the rate of fluid mixing*, J. Fluid Mech., 317 (1996), pp. 179–193.

[16] C. Wunsch and R. Ferrari, *Vertical mixing, energy, and the general circulation of the oceans*, Ann. Rev. Fluid Mech., 36 (2004), pp. 281–314.